



XXIII International Workshop on HEP and QFT
Yaroslavl, Russia, June 26 – July 3, 2017



Highlights from STAR heavy ion program

Vitalii A. Okorokov
(for the STAR Collaboration)

*National Research Nuclear University - MEPhI
(Moscow Engineering Physics Institute)*

Outline

1. Introduction

2. Selected recent results and plans

- Soft physics
- Heavy flavors at RHIC
- Neutral probes and jets
- Future perspectives

3. Summary

Key tasks for HIC program

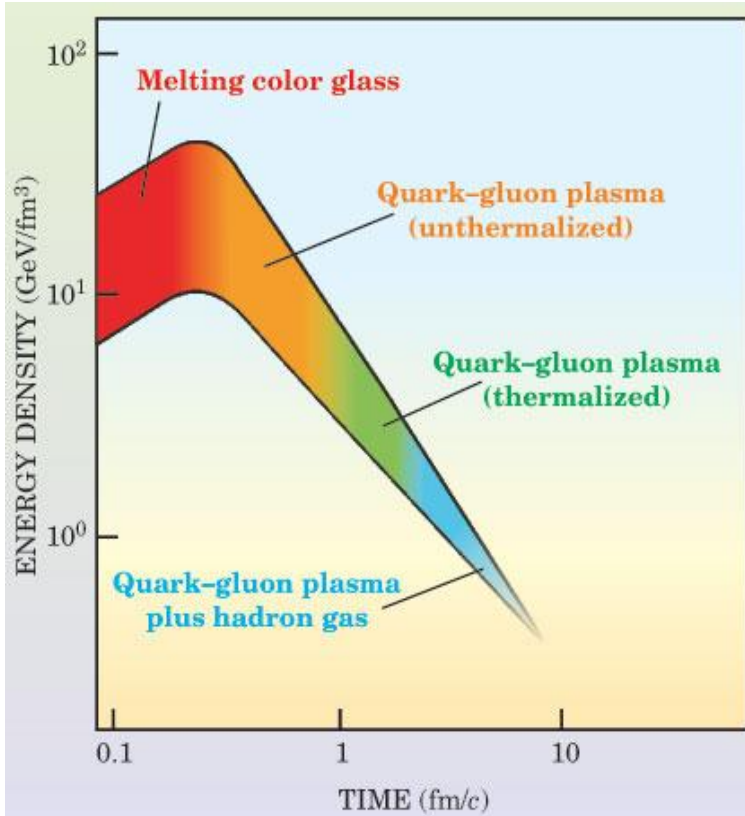


*Fig. 1. Cartoon for evolution of strongly interacting matter in HIC.
Phys. Today 10, 48 (2003).*

Numerous experimental results have suggested that nucleus-nucleus collisions produce hot matter consisting of deconfined quark and gluons. This new state of matter behaves like (quasi)ideal quark-gluon liquid and the matter is called strongly-coupled quark-gluon plasma (sQGP). The sQGP is observed in wide energy domain, at least for $\sqrt{s_{NN}} \geq 39$ GeV.

1. Key questions under discussion:

- properties of sQGP,
- features of QCD phase diagram.

2. Key problems outside the talk:

- exotic particles and antimatter, CNM effects,
- novel properties of QCD symmetries,
- spin physics in heavy ion collisions.

RHIC facility

Relativistic Heavy Ion Collider

1. The complex was designed and was built for investigations in QCD field specially.

2. **17** successful physics runs since 2000 year.

3. Experiments:

- large STAR continue to collect new data,

- small BRAHMS and PHOBOS were finished some years ago, large PHENIX completed the data taking in 2016.

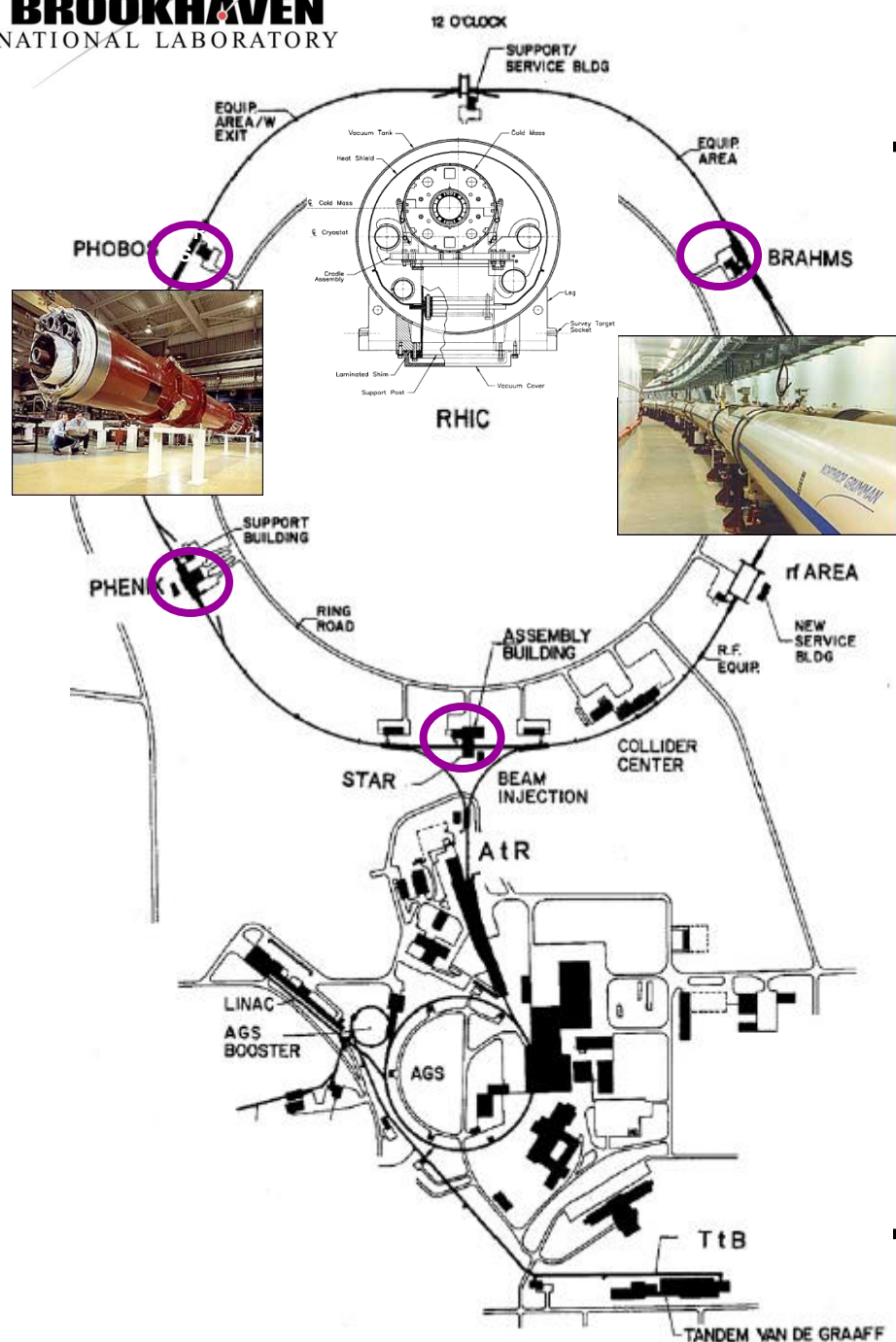


Fig. 2. RHIC. NPA 499, 235 (2003).

STAR detector

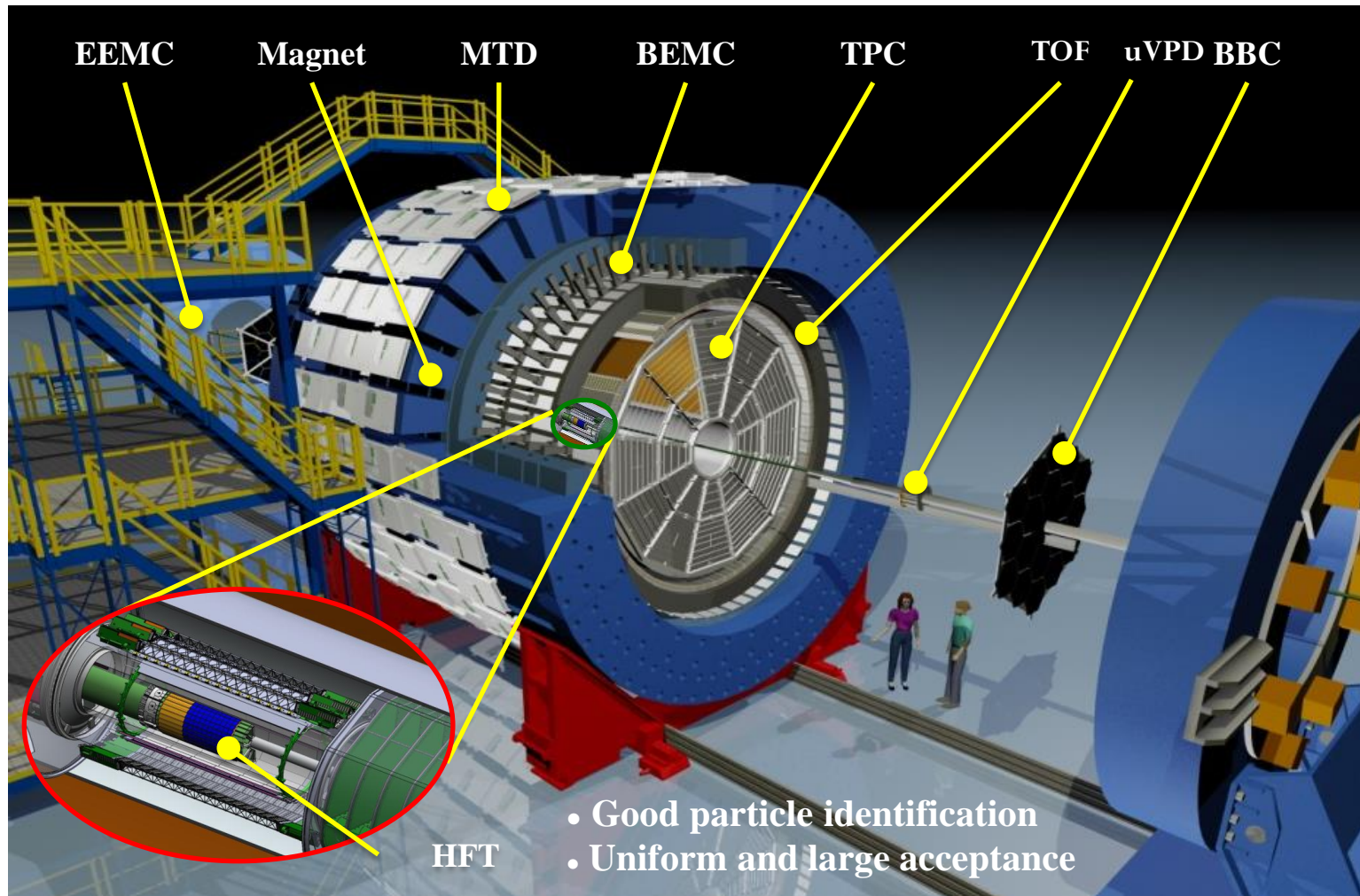


Fig. 3. General view of the STAR detector.

STAR: data collection

The data samples taken by STAR experiment since 2000 are shown in Table 1.

Table 1. Data samples.

Species	$\sqrt{s_{NN}}$, GeV
$p + p^a$	22.0 ^b , 62.4, 200, 410 ^b , 500, 510
$p + \text{Al}$	200
$p + \text{Au}$	200
$d + \text{Au}$	19.6, 39.0, 62.4, 200
$^3\text{He} + \text{Au}$	200
$\text{Al} + \text{Au}$	200
$\text{Cu} + \text{Cu}$	22.4 ^b , 62.4, 200
$\text{Cu} + \text{Au}$	200
$\text{Au} + \text{Au}$	4.5 ^{b,c} , 7.7, 9.2 ^b , 11.5, 14.5, 19.6, 27.0, 39.0, 55.4 ^b , 55.8 ^b , 62.4, 130, 200
$\text{U} + \text{U}$	193

Note: ^awith unpolarized ($\sqrt{s} = 62.4$ GeV) and with longitudinal / transverse polarized beams; ^brun with small integral luminosity, ^crun in fixed target mode

Event shape: observables

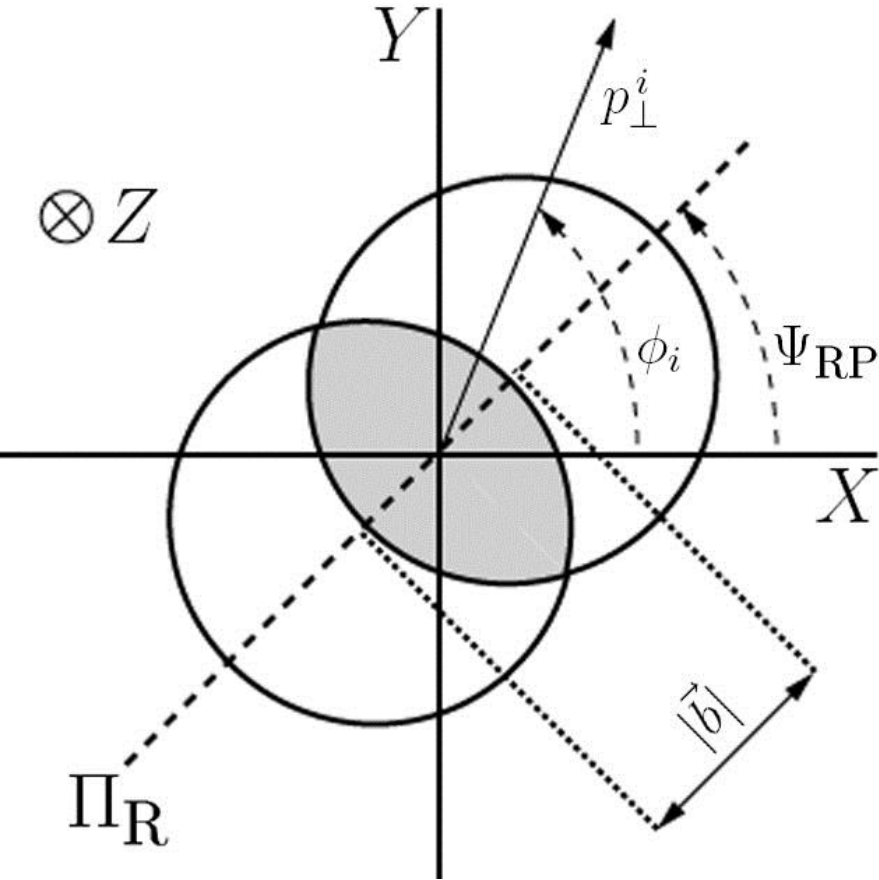


Fig. 4. Schematic image for non-central A+B collisions.

Definition:

the reaction plane – plane contains the beam axis and vector of impact parameter.

Fourier expansion of the triple differential invariant distribution for particles of some i type:

ZPC 70, 665 (1996); PRC 70, 057901 (2004).

$$E \frac{d^3 N_i}{d\vec{p}} \propto 1 + 2 \sum_{n=1}^{\infty} \sum_{j=1}^2 k_{j,n}^i F_j(n\Delta\phi_{RP}^i),$$

$$F_{1[2]}(x) \equiv \cos[\sin](x),$$

$$\Delta\phi_{RP}^i = \phi_i - \Psi_{RP}, \quad \phi_i = \tan^{-1}(p_y^i / p_x^i),$$

$$k_{1,n}^i \equiv v_n^i = \langle \cos[n\Delta\phi_{RP}^i] \rangle,$$

$$k_{2,n}^i \equiv a_n^i = \langle \sin[n\Delta\phi_{RP}^i] \rangle.$$

- v_n – collective flow – indicates the strength of P-even collectivity,

- a_n characterizes the strength of P-odd correlations.

Low-order v_n Fourier coefficients

Up to the present time, the main efforts are focused on the study of the low-order v_n coefficients due to their sensitivity to the key features of the final-state matter.

Table 2. Low-order azimuthal anisotropies.

n, symb.	title	main purpose / meaning	some refs.
1, v_1	directed flow	sensitivity to the EoS of the medium, possible probe of a QGP phase transition	<i>PRC 58, 1671 (1998); PLB 458, 454 (1999); PRC 61, 024909 (2000)</i>
2, v_2	elliptic flow	sensitivity to the shear viscosity over entropy density ratio η/s , probe of FS matter evolution including the hadronic phase	<i>PRL 73, 2532 (1994); Rel. Heavy Ion Phys. 23, 5 (2010); Annu.Rev.Nucl. Part.Sci. 63, 123 (2013)</i>
3, v_3	triangular flow	sensitivity to the presence of a low viscosity QGP phase, important probe of early plasma phase	<i>PRC 88, 064908 (2013); PLB 720, 352 (2013); PLB 753, 506 (2016)</i>

Nuclear modification factor

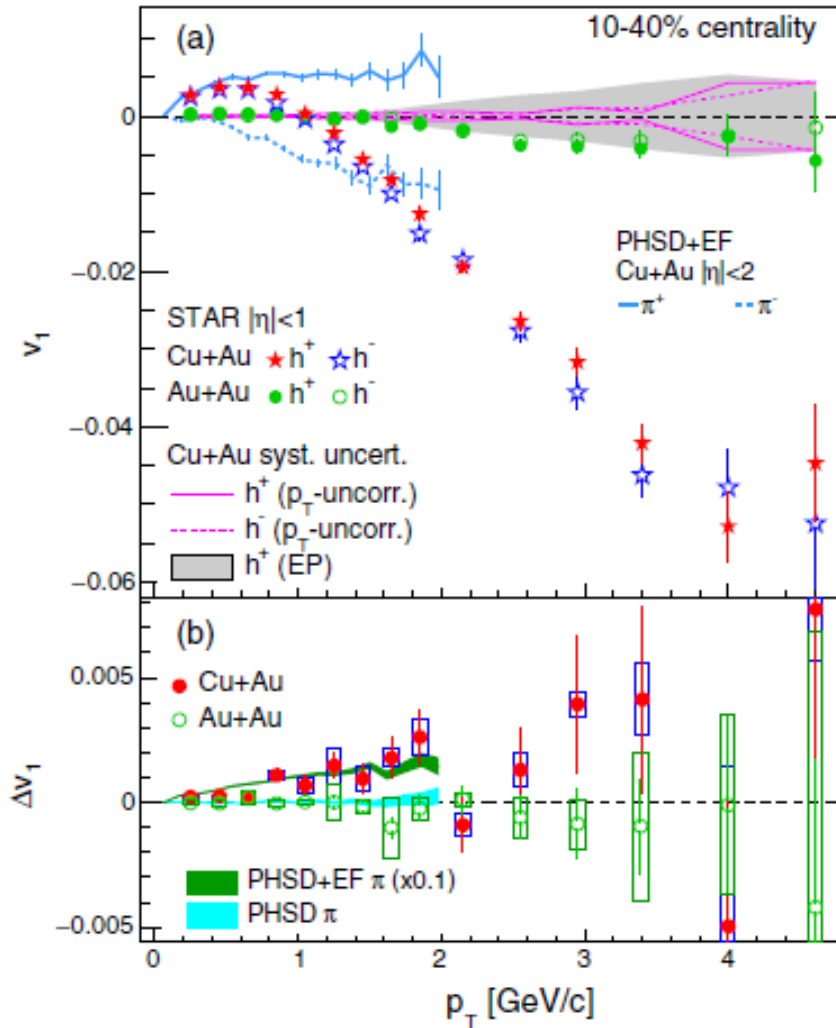
Definition:

the nuclear modification factor R_{AA} – ratio of the number of some particles measured in A+A collisions to the yield in $p+p$ collisions scaled by the average number of binary nucleon-nucleon collisions.

$$\begin{aligned} R_{AA}(p_T) &= \frac{1}{\langle N_{\text{bin}} \rangle} \frac{d^2 N^{AA} / dp_T d\eta}{d^2 N^{pp} / dp_T d\eta} = \\ &= \frac{1}{\langle N_{\text{bin}} \rangle / \sigma_{\text{inel}}^{pp}} \frac{d^2 N^{AA} / dp_T d\eta}{\sigma_{\text{inel}}^{pp} d^2 N^{pp} / dp_T d\eta} = \\ &= \frac{1}{T_{AA}} \frac{d^2 N^{AA} / dp_T d\eta}{d^2 \sigma^{pp} / dp_T d\eta}, \end{aligned}$$

where T_{AA} is the nuclear overlap function.

v_1 in asymmetric collisions



A finite difference in v_1 between positive and negative charged particles was observed in the kinematic domain of $0.15 < p_T < 2$ GeV/c and $|\eta| < 1$. The Δv_1 seems to increase with p_T . The v_1 results from Au+Au collisions show much smaller values compared to those in Cu+Au.

These results are consistent with the presumption of a strong, initial electric field in asymmetric collisions. The p_T dependence of Δv_1 is qualitatively described by the parton-hadron-string-dynamics (PHSD) model at $p_T < 2$ GeV/c. However, the magnitude of Δv_1 is smaller by a factor of 10 than the model predictions. This may indicate that most of the quarks and antiquarks have not yet been created within the lifetime of the electric field ($t \leq 0.25$ fm/c).

Fig. 5. v_1 of positive and negative particles (top) and the difference between the two spectra (bottom) as a function of p_T in Cu+Au and Au+Au collisions. The PHSD model calculations for π^\pm with and without the initial electric field (EF) in the same centrality region are presented for comparison. PRL 118, 012301 (2017).

v_2 of light flavors

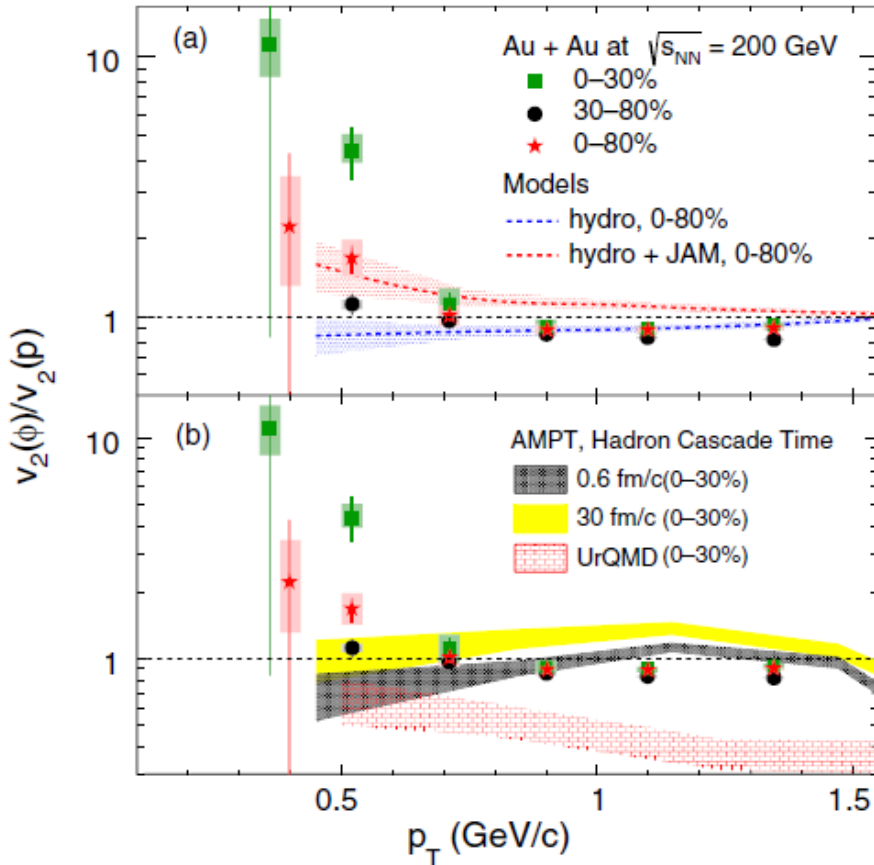


Fig. 6. $v_2(\phi)/v_2(p)$ ratio as a function of p_T for various centrality bins. Shaded boxes are the systematic uncertainties, vertical lines are statistical errors. The bands in (a) and (b) are the hydro model and transport model calculations.

PRL 116, 062301 (2016).

The $v_2(\phi)/v_2(p)$ ratios are larger than unity at $p_T \sim 0.5$ GeV/c for most central 0–30% bin showing an indication of breakdown of the expected mass ordering in that momentum range. This could be due to a large effect of hadronic rescattering on the proton v_2 .

The $v_2(\phi)/v_2(p)$ increases with increasing hadronic cascade time (bottom panel). This is attributed to a decrease in the $v_2(p)$ due to an increase in hadronic rescattering, while the ϕ -meson v_2 remains unaffected.

The ratio from UrQMD is much smaller than unity. The UrQMD model lacks partonic collectivity and therefore does not fully develop the ϕ -meson v_2 .

BES for v_2 of light (anti)nuclei

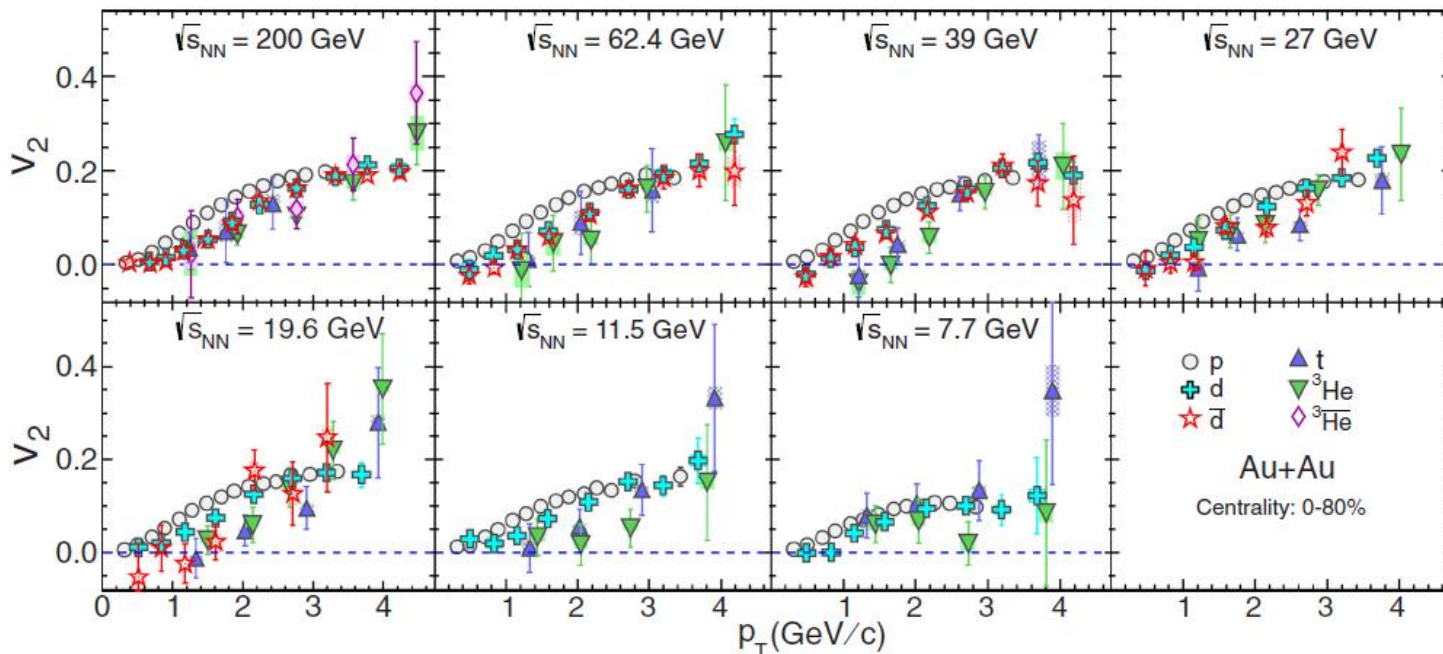


Fig. 7. Midrapidity $v_2(p_T)$ for light nuclei from minimum bias Au+Au collisions in comparison with elliptic flow for protons. Lines and boxes at each marker represent statistical and systematic errors, respectively. PRC 94, 034908 (2016).

Similar to hadrons over the measured p_T range, light-(anti)nuclei $v_2(p_T)$ show a monotonic rise with increasing p_T , mass ordering at low p_T , and a reduction for more central collisions.

It is observed that v_2 of nuclei and antinuclei are of similar magnitude for $\sqrt{s_{NN}} \geq 39$ GeV.

v_2 of light nuclei: A-scaling

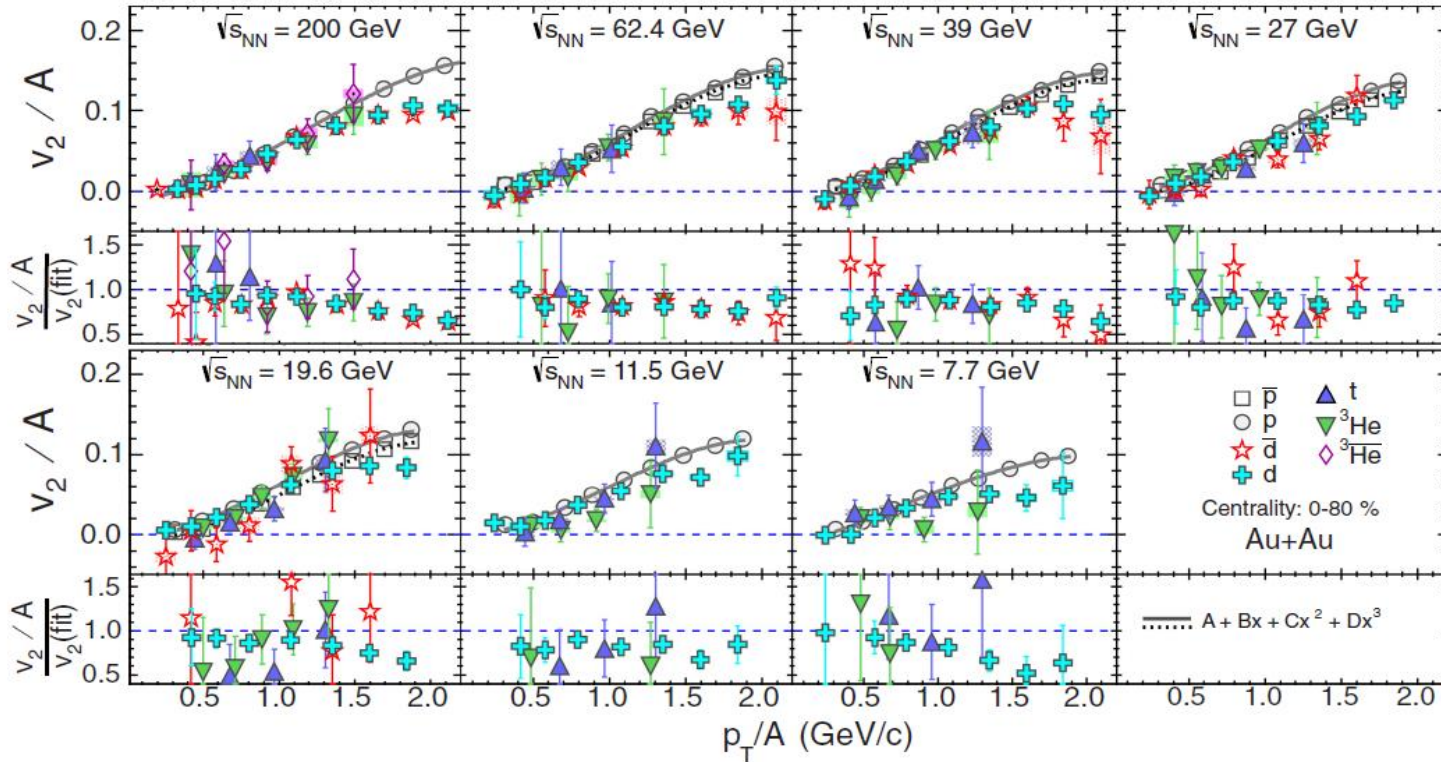
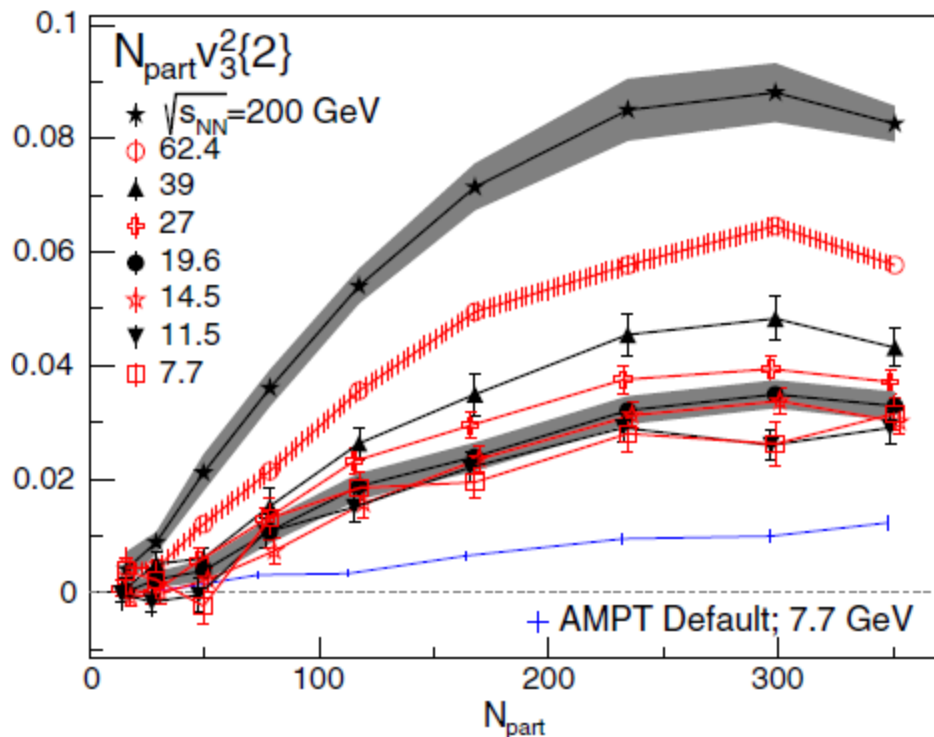


Fig. 8. Midrapidity $v_2(p_T)$ for light (anti)nuclei from minimum bias Au+Au collisions in comparison with v_2 for (anti)protons. Gray solid (black dotted) lines correspond to third order polynomial fits to the (anti)proton v_2 data. The ratios of $[v_2/A]/\text{fit}$ are shown in the lower panels at each corresponding collision energy. PRC 94, 034908 (2016).

In general the light-nuclei v_2 follow an atomic mass number scaling indicates that the coalescence of nucleons might be the underlying mechanism of light-nuclei formation in HIC. This fact is corroborated by model calculations.

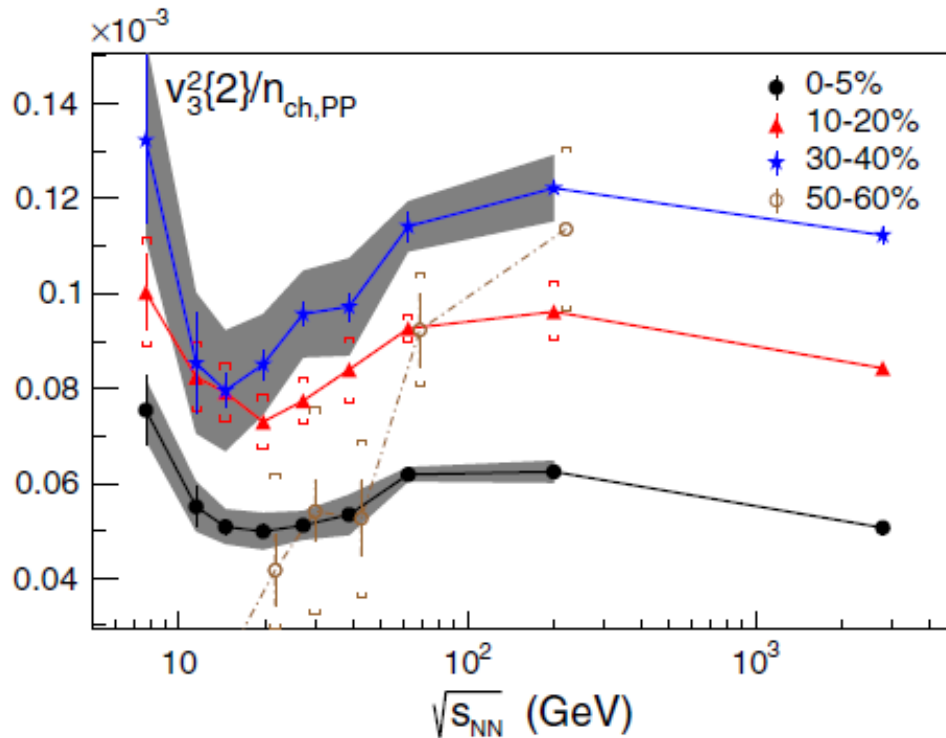
Centrality dependence of v_3



For sufficiently central collisions ($N_{\text{part}} > 50$), the v_3 persist down to the lowest energies studied. For more peripheral collisions, however, the correlation appears to be absent at low energies for $N_{\text{part}} < 50$, in agreement with AMPT model. This non-QGP model predicts a smaller v_3 value than the data, suggesting that a QGP phase may exist in more central collisions at $\sqrt{s} = 7.7$ GeV.

Fig. 9. The $v_3^2\{2\}$ results from Au+Au collisions integrated over all $\Delta\eta$ and multiplied by N_{part} . Statistical errors are within the symbol size. Systematic errors are shown either as a shaded band or as thin vertical error bars with caps. The v_3 from a non-QGP-based model, AMPT, is also shown for $\sqrt{s_{\text{NN}}} = 7.7$ GeV for comparison.
PRL 116, 112302 (2016).

Energy dependence of v_3



When divided by multiplicity, v_3 shows a local minimum at $\sqrt{s} = 15-20$ GeV in centrality range from 0% to 50%. This feature has not been shown in any known models of HIC and could indicate an interesting trend in the pressure developed inside the system.

Fig. 10. $v_3^2\{2\}$ divided by the midrapidity, charged-particle multiplicity density per participant pair in Au+Au and Pb+Pb (2.76 TeV) collisions. Systematic errors are shown either as a shaded band or as thin vertical error bars with caps. PRL 116, 112302 (2016).

Global hyperon polarization

Non-central nuclear collisions have angular momentum on the order of $10^3\hbar$, and shear forces generated by the interpenetrating nuclei may generate a clear vortical structure.

The (anti) Λ are used to measure the global hyperon polarization in non-central Au+Au collisions because they are “self analyzing”, i.e. in the decay

$$\Lambda \rightarrow p\pi^-,$$

the p tends to be emitted along the spin direction of the parent Λ . At present due to the limited statistics, only the average projection of polarization on overall angular momentum was extracted.

BES for (anti) Λ polarization

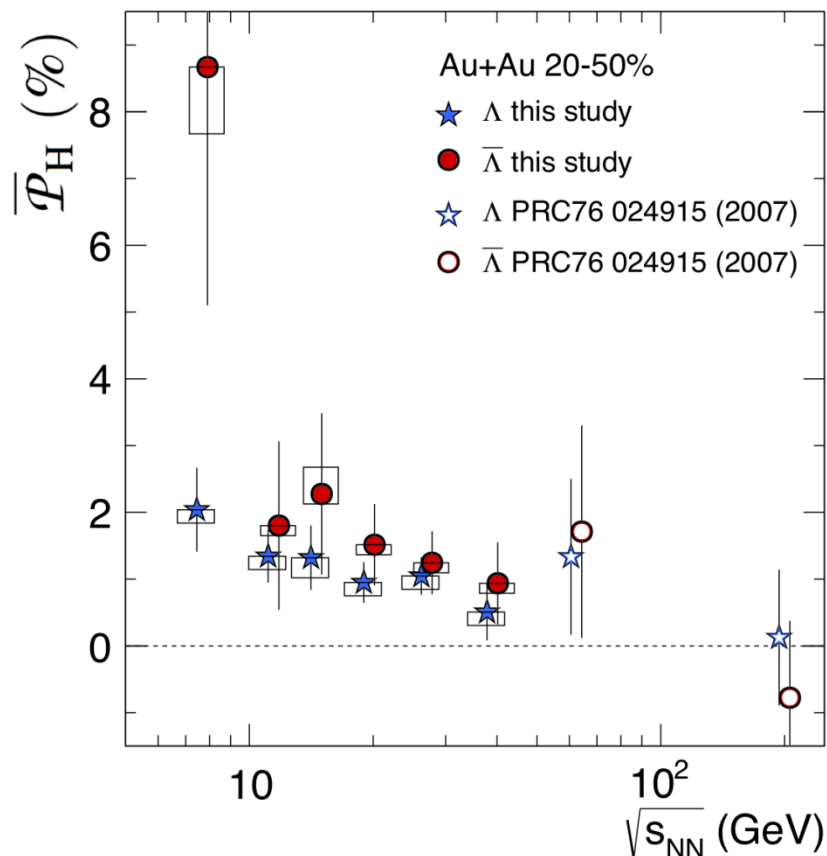


Fig. 11. The average polarization for $H = (\text{anti})\Lambda$ hyperons from semi-central Au+Au collisions as a function of collision energy. Only statistical errors are shown for the results of the present study ($\sqrt{s_{NN}} > 40$ GeV). Boxes indicate systematic uncertainties.
arXiv: 1701.06657 [nucl-ex], 2017.

At $\sqrt{s_{NN}} < 200$ GeV, a positive polarization is observed for (anti) Λ hyperons. The data are statistically consistent with the hypothesis of energy-independent polarizations of 1.08 ± 0.15 (1.38 ± 0.30) percent for (anti) Λ .

The $\sqrt{s_{NN}}$ -averaged polarizations indicate a vorticity of $\omega = (9 \pm 1) \times 10^{21} \text{ s}^{-1}$, which is estimated using the hydrodynamic relations and takes into account the “feed-down” contributions.

Study of heavy flavors: motivation

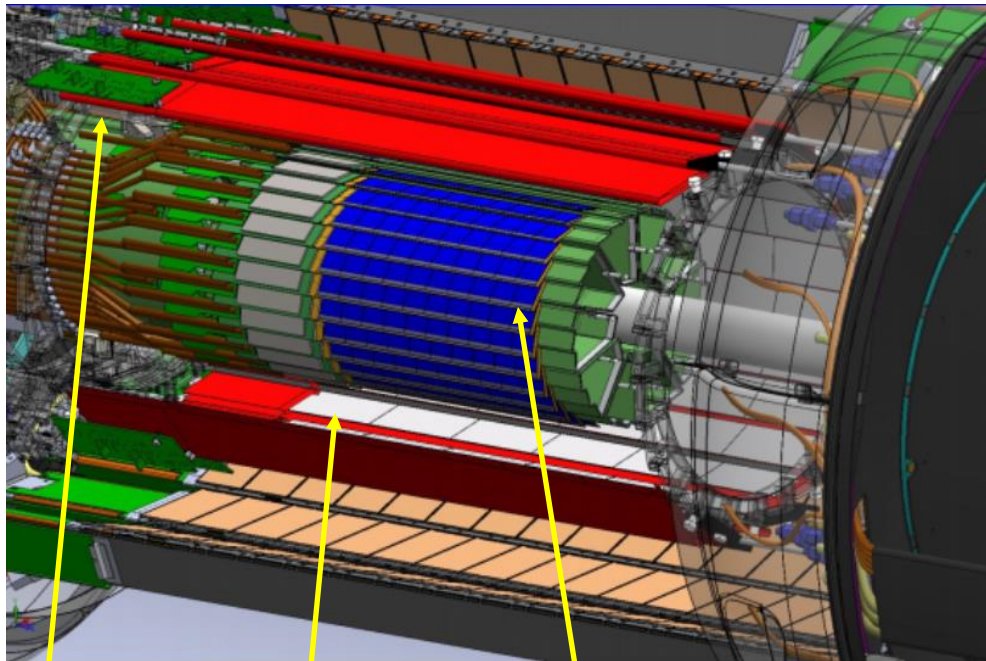
Heavy quark masses are mostly uncharged by chiral symmetry restoration.

Heavy flavor (HF) particles are produced early in collisions due to hard scattering processes. Therefore they allow the study of whole space-time evolution of sQGP.

Study of heavy quark diffusion is essential for better understanding of transport properties of sQGP and underlying fluid of light partons.

Precise measurements of c- and b-quarks energy loss are crucial for understanding of parton interactions with the hot environment.

STAR heavy flavor tracker



SSD
at 23 cm

IST
at 14 cm

PXL
at 2.5 and 8 cm

Fig. 12. STAR HFT includes pixel detector (PXL), intermediate silicon tracker (IST) and silicon strip detector (SSD).

The HFT is the newest member of the STAR detector subsystems. It is made using thinned monolithic active pixel sensor technology.

The HFT is characterized by low material budget and large acceptance coverage ($|\eta| < 1$, $0 < \phi < 2\pi$).

The HFT makes it possible for the first time to directly track the decay products of hadrons comprised of charm and bottom quarks with high pointing resolution ($\sim 30 \mu\text{m}$ for particles with $p \geq 1.5 \text{ GeV}/c$).

D^0 azimuthal anisotropy

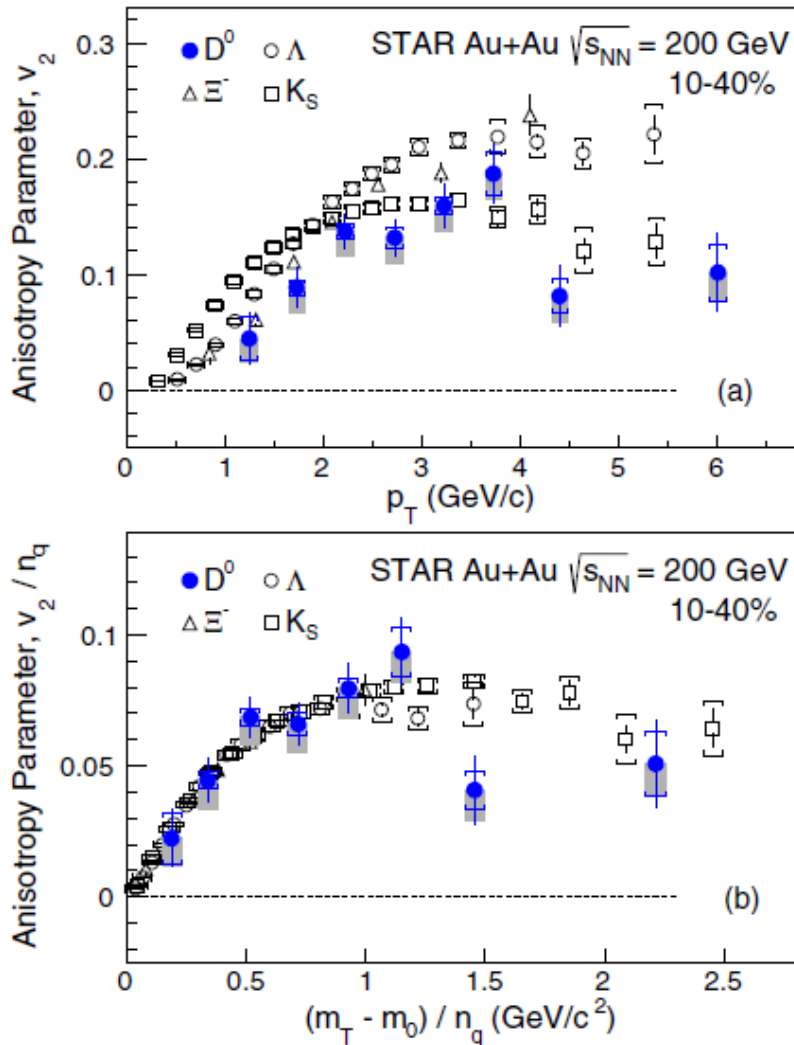


Fig. 13. (a) v_2 as a function of p_T and (b) v_2/n_q dependence on $(m_T - m_0)/n_q$ for D^0 compared with earlier measurements for strange particles. The vertical bars and brackets represent statistical and systematic uncertainties, respectively, and the gray bands represent the estimated nonflow contribution. PRL 118, 212301 (2017).

There is a clear mass ordering for $p_T < 2$ GeV/c including D^0 mesons (a). For $p_T > 2$ GeV/c, the D^0 meson v_2 follows that of other light mesons indicating a significant c-quark flow at highest RHIC energy.

The D^0 v_2 falls into the same universal trend as all other light hadrons, in particular, for the range $(m_T - m_0)/n_q < 1$ GeV/c². This suggests that c-quarks have gained significant flow through interactions with the sQGP in the collisions under consideration.

HF v_2 : experiment vs models

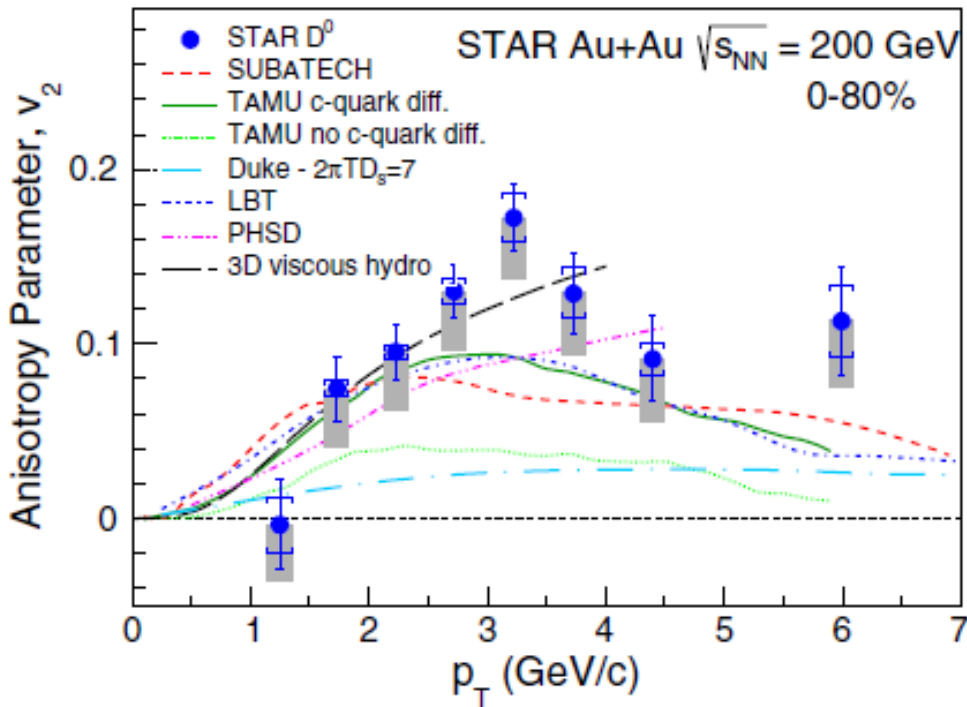


Fig. 14. v_2 as a function of p_T for D^0 in minimum bias Au+Au collisions compared with model calculations. *PRL* 118, 212301 (2017).

The TAMU model describes the data only with no c-quark diffusion. A 3D viscous hydrodynamic simulation with $\eta/s = 0.12$ tuned to describe v_2 for light hadrons predicts v_2 for D^0 that is consistent with data for $p_T < 4$ GeV/c. This suggests that c-quarks have achieved thermal equilibrium in these collisions.

The statistical significance test was performed for the consistency between data and each model quantified by χ^2/ndf . The 3D viscous hydro models shows the best $\chi^2/\text{ndf} = 0.73$ for the measured p_T region. The models that can describe both the R_{AA} and v_2 data include the temperature-dependent charm diffusion coefficient $\kappa \equiv 2\pi TD_s$ in the range of $\sim 2-12$. The κ predicted by lattice QCD calculations fall in the same range.

Υ Production in HI collisions

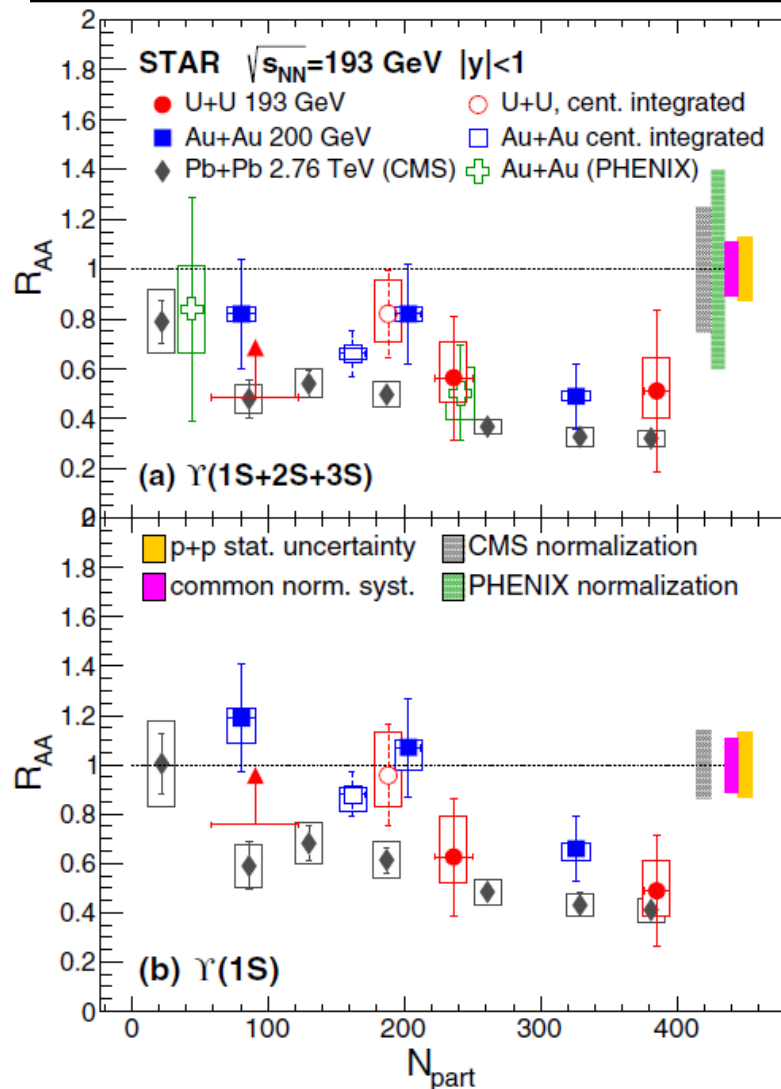


Fig. 15. $\Upsilon(1S+2S+3S)$ (a) and $\Upsilon(1S)$ (b) nuclear modification factor R_{AA} as a function of N_{part} in relativistic heavy ion collisions. The data points in the 30–60% centrality bin have large statistical and systematical uncertainties, providing little constraint on R_{AA} . Therefore the 95% lower confidence bound is only indicated for the 30%–60% centrality U+U data. PRC 94, 064904 (2016).

The trend marked by the points $R_{AA}(N_{part})$ for Au+Au is confirmed by the U+U data. There is strong suppression of the $\Upsilon(2S+3S)$ states in U+U as well as in Au+Au collision.

There is neither a significant difference between the results in any of the centrality bins, nor any evidence of a sudden increase in suppression in central U+U compared to the central Au+Au data. But one can note the precision of the current measurement does not exclude a moderate drop in R_{AA} .

Υ suppression: experiment vs models

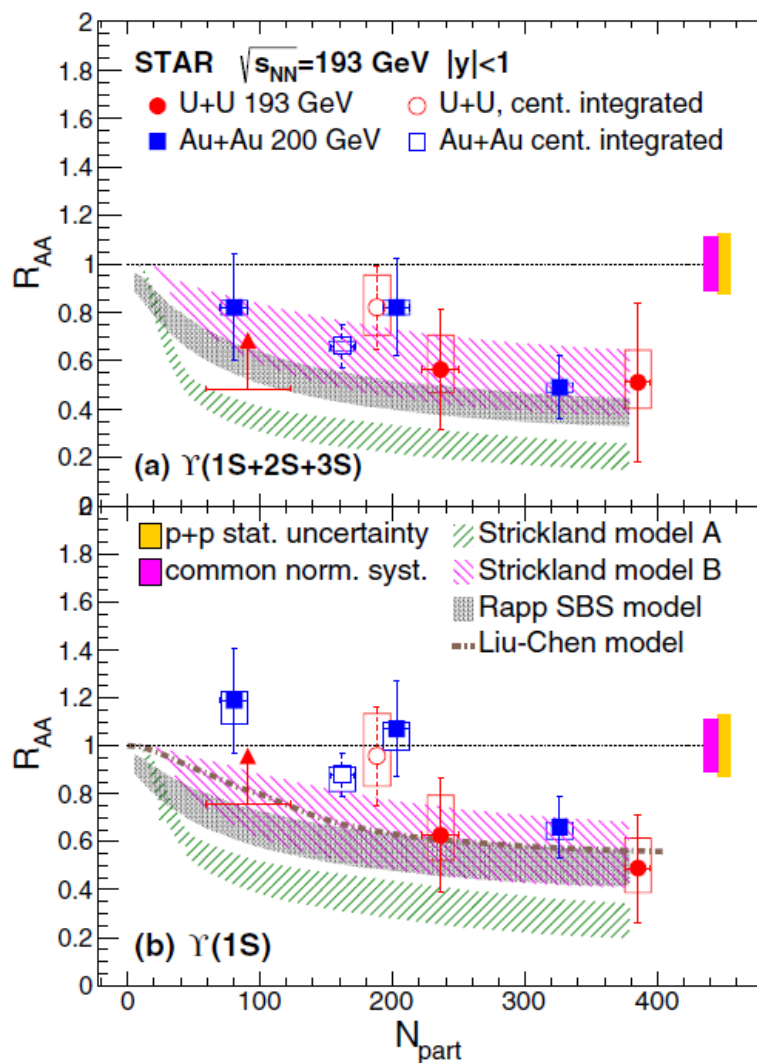


Fig. 16. $\Upsilon(1S+2S+3S)$ (a) and $\Upsilon(1S)$ (b) R_{AA} vs N_{part} in $\sqrt{s_{NN}} = 193$ GeV U+U collisions, compared to different models. The 95% lower confidence bound is indicated for the 30%–60% centrality U+U data. PRC 94, 064904 (2016).

The Rapp model included CNM effects, dissociation of bottomonia in the hot ($T = 330$ MeV) medium and regeneration for strongly bound scenario (SBS) for the internal-energy-based heavy quark potential describe the STAR data within uncertainties as well as other internal-energy-based models with an initial central temperature $428 < T < 442$ MeV (“model B”) and $T = 340$ MeV (“Liu-Chen model”).

The “model A” with the free-energy-based potential corresponding to a more weakly bound scenario (WBS) tends to underpredict the R_{AA} especially for the $\Upsilon(1S)$.

R_{AA} for quarkonia in HI collisions

Nominal binding energy is equal to the following difference $2m_{D(B)} - m_{J/\psi(Y)}$.

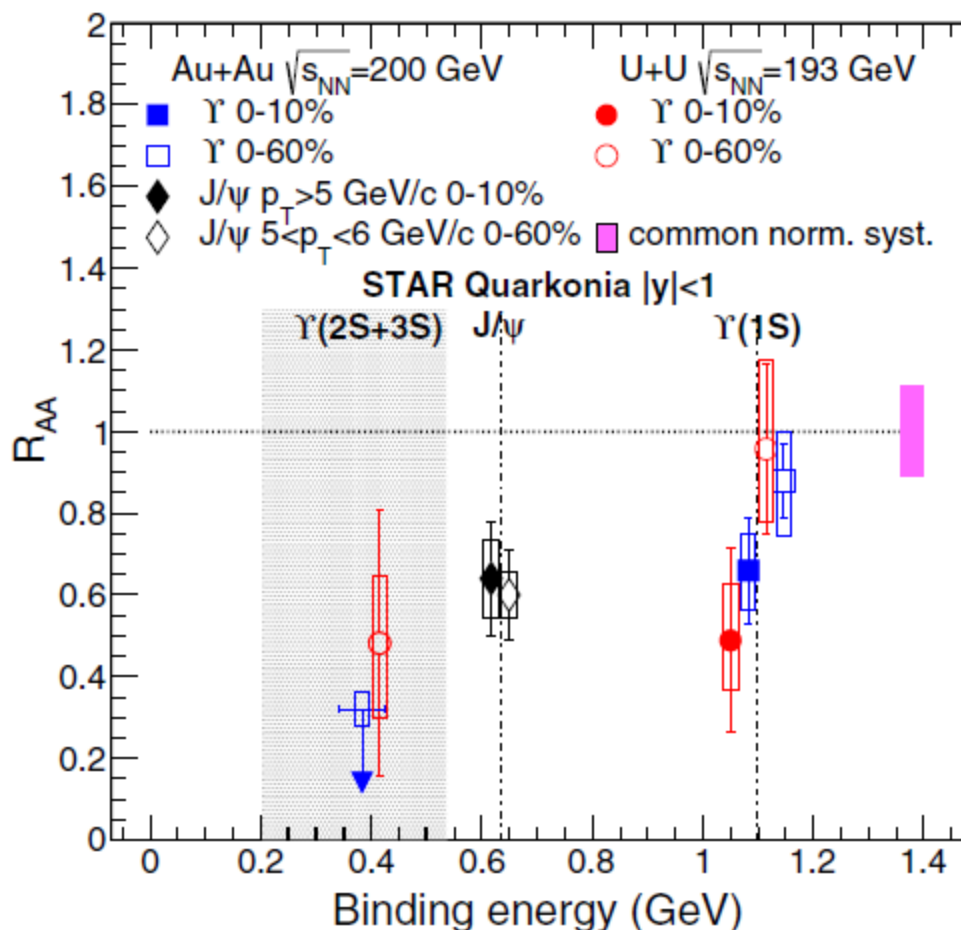
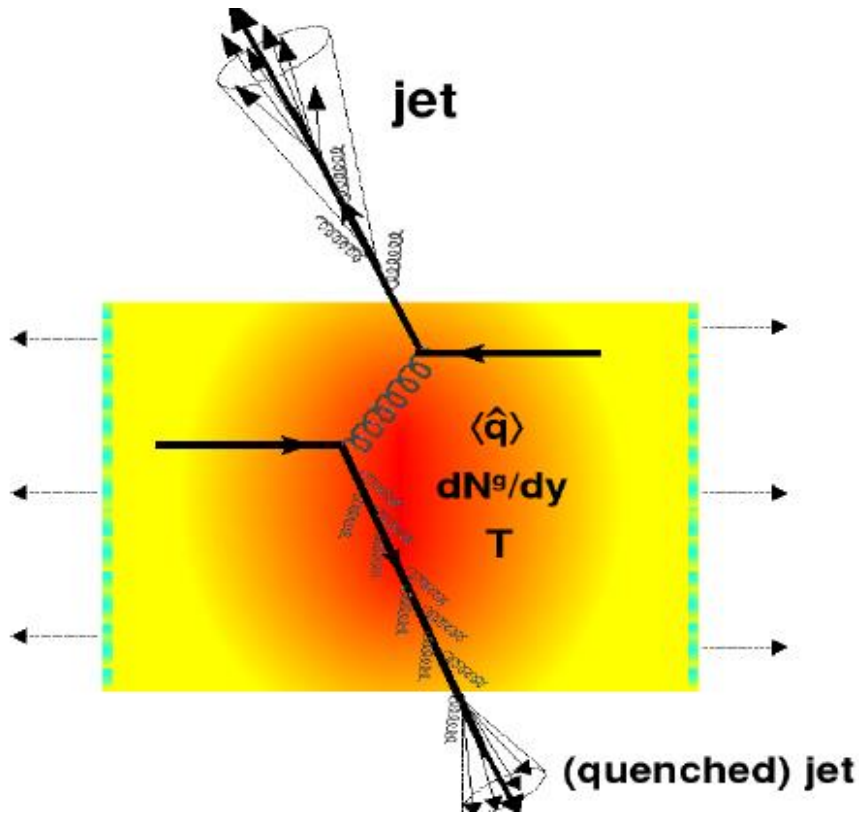


Fig. 17. Quarkonium R_{AA} versus binding energy in Au+Au and U+U collisions. Open symbols represent 0–60% centrality data; filled symbols are for 0–10% centrality. A blue horizontal line indicates a 95% upper confidence bound. The black diamonds mark the high- p_T J/ψ measurement. The vertical lines represent nominal binding energies for the $Y(1S)$ and J/ψ . The shaded area spans between the binding energies of $Y(2S)$ and $Y(3S)$. PRC 94, 064904 (2016).

The results in U+U collisions are consistent with the Au+Au measurements as well as with the expectations from the sequential melting hypothesis.

Jets in hot environment



Jet quenching is considered as one of the most promising signatures of formation of sQGP and sensitive probe for transport properties of final-state matter.

Study of jet quenching with various type triggers is considered as important tool for detailed investigation of transport properties of sQGP.

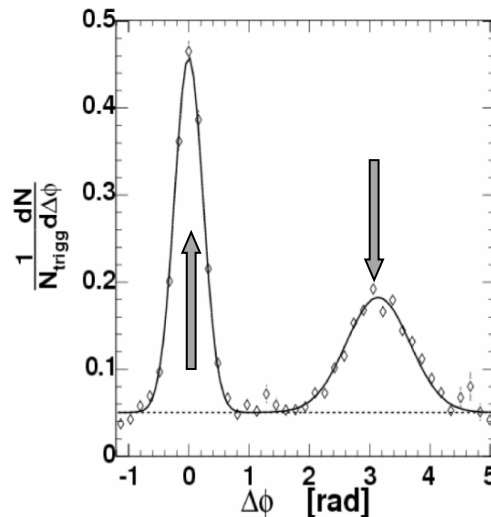
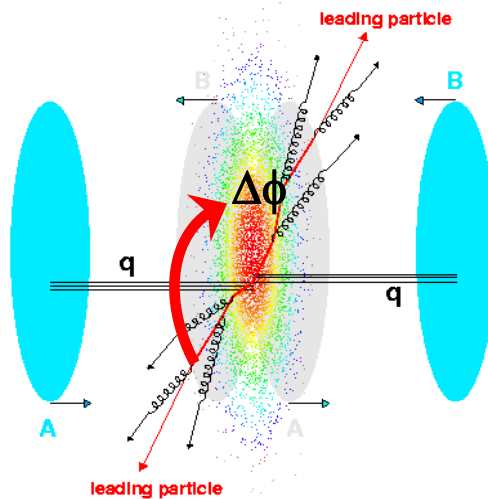
There are two experimental techniques for jet studies: (i) with help of azimuthal correlations, (ii) via full jet reconstruction.

Fig. 18. Schematic image for quenching of hadron jet passes through hot quark-gluon matter.

Two-particle $\Delta\phi$ -correlations (basis)

1. The particle with high p_T is selected in event – trigger particle; then pairs «trigger particle + associated particle» are formed and $\Delta\phi = \Delta\phi_t - \Delta\phi_a$ are calculated.
2. As expect, correlations appear at $\Delta\phi \approx 0$ – the peak for small relative azimuthal angles – corresponds to jet in which the both trigger and associated particles are fragmentation products of one parton; $\Delta\phi \approx \pi$ – the peak in the region of large relative azimuthal angles – corresponds to jet in which the trigger and associated particles are fragmentation products of different (back-to-back) partons.

$$C_2(\Delta\phi) = N_{\text{trigg}}^{-1} \int d(\Delta\eta) N(\Delta\phi, \Delta\eta), \quad Y = \int d(\Delta\phi) C_2(\Delta\phi)$$



C_2 – two-particle azimuthal correlation function,

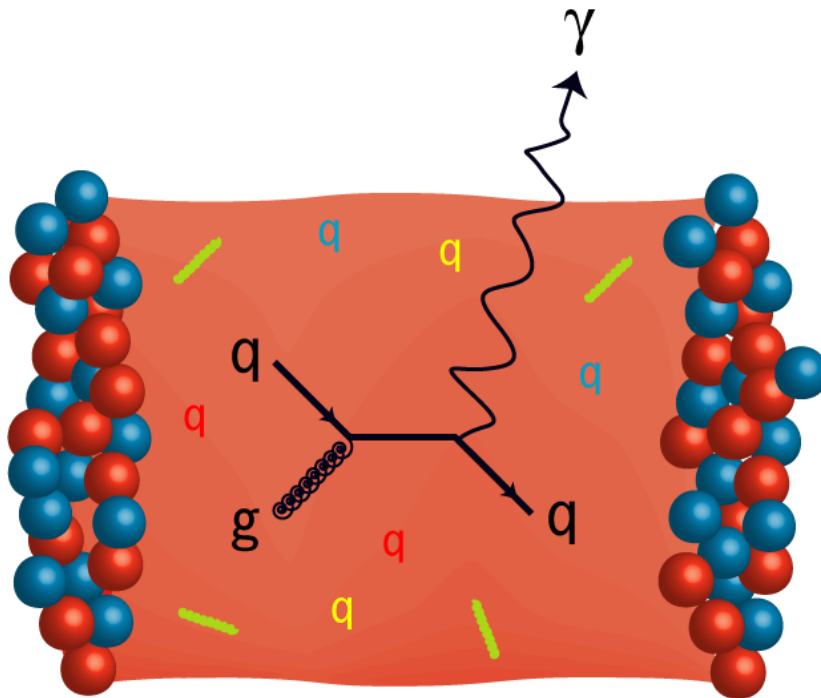
Y – the per-trigger yield of particle pairs.

Fig. 19. Scheme for di-jet event structure in ion collision (left), example of $C_2(\Delta\phi)$ for pp collisions (right) from PRD 74, 072202 (2006).

Neutral probes for sQGP

Forty years ago [*Nuv. Cim. A34 (1976) 391*] it was pointed out that direct photons (real or virtual) are penetrating probes for the bulk matter produced in hadronic collisions, as

- (i) they do not interact strongly,
- (ii) they have a large mean free path.



The physics analyses are focused on the direct γ yield and on azimuthal correlations with neutral triggers (γ and π^0) produced in nucleus-nucleus collisions.

Fig. 20. Schematic image for γ production in strongly interacting environment.

Direct γ spectra

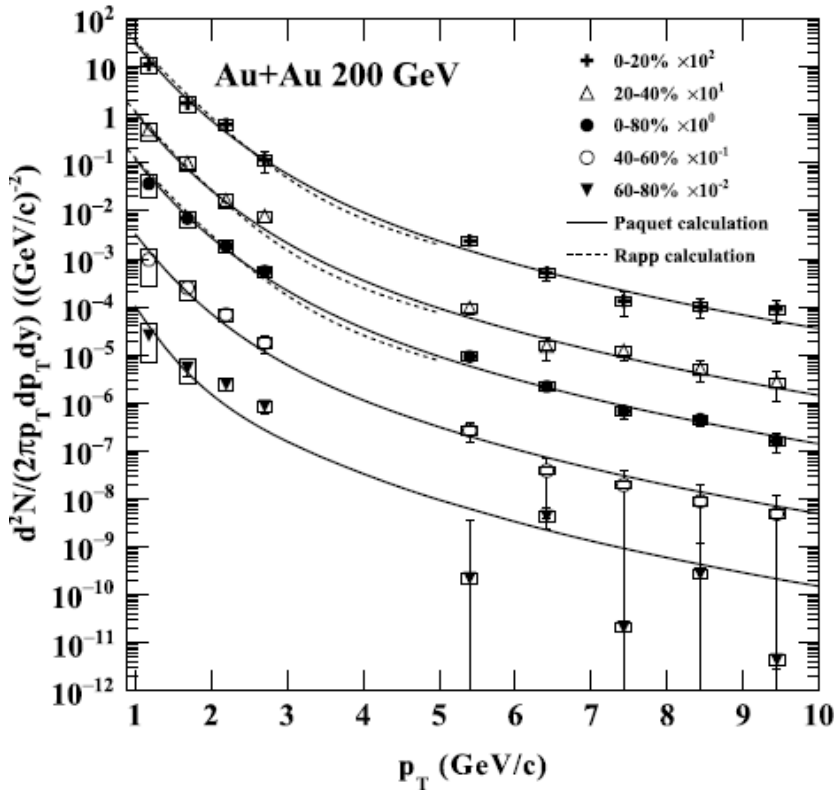


Fig. 21. The direct γ invariant yield as a function of p_T in comparison with model predictions. The statistical and systematic errors are shown by bars and boxes, respectively.
 PLB 770, 451 (2017).

The direct virtual γ invariant yields at mid-rapidity are derived in the ranges $1 < p_T < 3$ GeV/c and $5 < p_T < 10$ GeV/c.

A clear excess in the γ_{dir} invariant yield is observed in comparison with the nuclear overlap function T_{AA} scaled $p+p$ reference the p_T range $1 < p_T < 3$ GeV/c. For $p_T > 6$ GeV/c the production follows T_{AA} scaling.

Model calculations with contributions from thermal radiation and initial hard parton scattering are consistent within experimental uncertainties with the γ_{dir} invariant yield in 0–20%, 20–40% and 40–60% centrality bins. In 60–80% collisions there is systematic excess data over model curve at $2 < p_T < 3$ GeV/c.

π^0/γ – h^\pm Azimuthal correlations

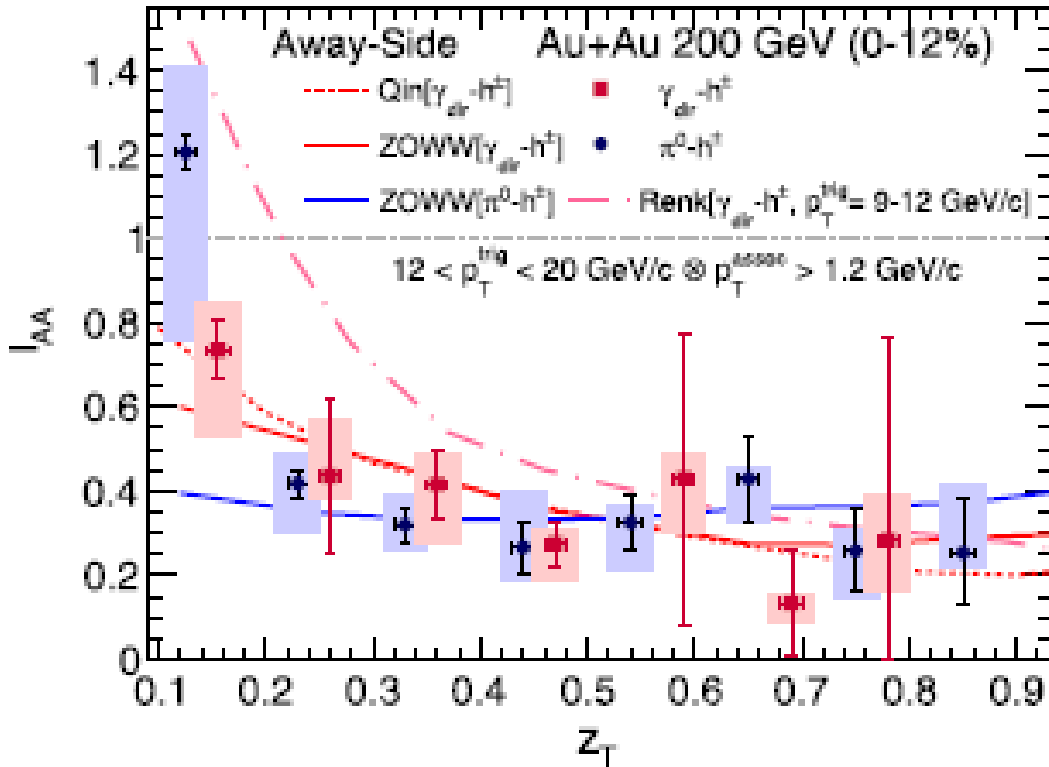


Fig. 22. z_T -dependence of I_{AA} for π^0 and γ triggers (the points are slightly shifted for visibility) in most central Au+Au collisions. The vertical lines are statistical errors, vertical extent of the boxes – systematic uncertainties. The curves represent the model predictions. PLB 760, 689 (2016).

$$I_{AA}(z_T) = Y^{AA}(z_T) / Y^{pp}(z_T),$$

$$z_T \equiv p_T^a / p_T^{tr},$$

Y – the per-trigger yield in AA (pp) collisions. It is expected $I_{AA} = 1$ in the absence of medium modification.

I_{AA} for both π^0 and γ_{dir} triggers show
 - indication on less suppression at low $z_T \in (0.1; 0.2)$ than at high z_T ;
 - similar levels of suppression.

There is no manifestation of the expected differences due to the color-factor effect and the difference in average path lengths between π^0 and γ_{dir} triggers (path-length dependence).

Full jet reconstruction

The development of experimental technique and data analysis results in the possibility for full reconstruction of hadron jets in nucleus-nucleus collisions. At present fully reconstructed jets are one of the main tools to constrain the medium transport parameters.

In STAR the anti- k_T algorithm with $R = 0.2, 0.5$ ($R^2 = [\Delta\phi]^2 + [\Delta\eta]^2$) and a low IR-cutoff ($p_T > 0.2$ GeV/ c) is used for full jet reconstruction from charged tracks in Au+Au collisions. STAR measures the semi-inclusive distributions of reconstructed charged particle jets recoiling from a high p_T trigger hadron

$$\frac{1}{N_{\text{trig}}^h} \frac{d^2 N_j}{dp_{T,j} d\eta_j} = \frac{1}{\sigma^{AA \rightarrow h+X}} \frac{d^2 \sigma^{AA \rightarrow h+jet+X}}{dp_{T,j} d\eta_j}.$$

Here η_j is the pseudo-rapidity of jet centroid, $\sigma^{AA \rightarrow h+X}$ is the cross-section to generate a trigger hadron, and $d^2 \sigma^{AA \rightarrow h+jet+X} / dp_{T,j} d\eta_j$ is the double differential cross-section for coincidence production of a trigger hadron and a recoil jet, $AA \equiv p + p, \text{ Au+Au}$.

The combinatorial background is removed by mixed-event technique. This allows the access for low- p_T jets.

Semi-inclusive recoil jets

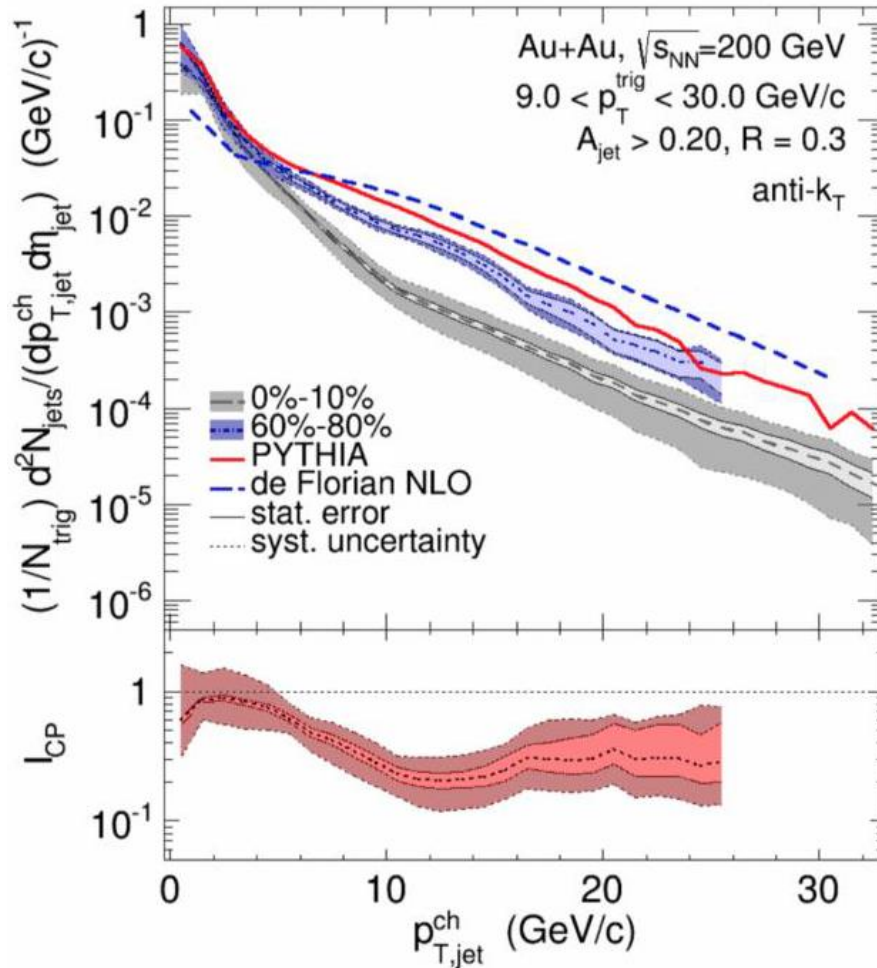


Fig. 23. Fully corrected distributions of $Y(p_{T,j})$ (upper) and its ratio I_{CP} (lower) for central and peripheral Au+Au collisions, for anti- k_T jets with $R = 0.3$ and area $A_{\text{jet}} > 0.2$. The upper panels also show yield for $p+p$ collisions, calculated using PYTHIA at the charged-particle level and NLO pQCD transformed to the charged-particle level. The uncertainty of the NLO calculation is not shown.
 arXiv: 1702.01108 [nucl-ex], 2017.

The I_{CP} shows a clear suppression of yields in central events for $p_{T,j} > 10$ GeV/c for all cone radii $R = 0.2, 0.3, 0.4$ and 0.5 under study.

The horizontal shifts in the range where the I_{CP} is flat ($10 < p_{T,j} < 20$) are $-6.3 \pm 0.6 \pm 0.8$ GeV/c and $-3.8 \pm 0.5 \pm 1.8$ GeV/c for $R = 0.3$ and $R = 0.5$, respectively. The suppression and shift, and their reduction for larger cones might indicate an out-of-cone energy transport by interaction of the jet with the medium, averaged over the recoil jet population.

Towards run 18: isobar collisions

STAR's highest scientific priority for Run 18 is the successful realization of the isobaric collision program (Rb+Rb, Zr+Zr at $\sqrt{s_{NN}} = 200$ GeV) for clarification the interpretation of measurements related to chiral effects, in particular chiral magnetic effect (CME).

Collisions of isobaric nuclei ($Z_{Rb} = 44, Z_{Zr} = 40$) present a unique opportunity to vary the initial magnetic field ($B \propto Z^2$) and then separate the CME-signal and the flow-related background.

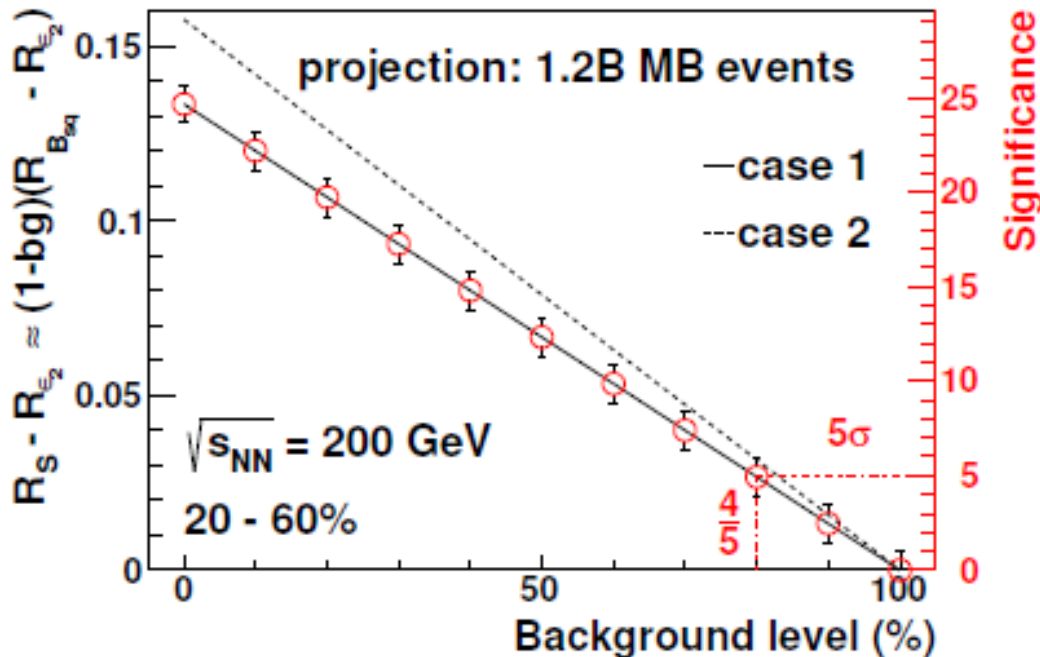
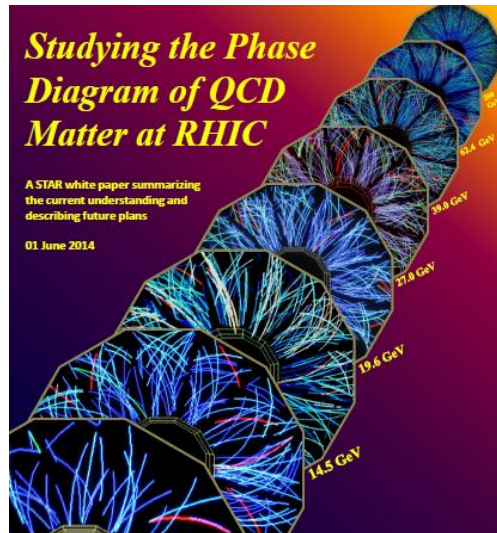


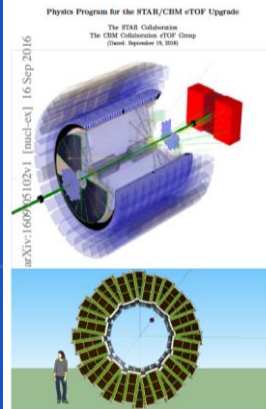
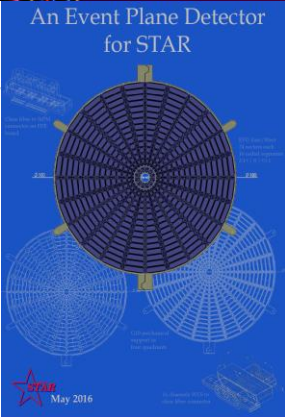
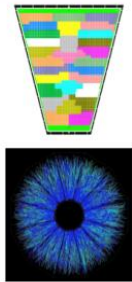
Fig. 24. Magnitude (l.s.) and significance (r.s.) of the relative difference in the CME signal between Ru+Ru and Zr+Zr, $R_S - R_{\epsilon_2}$ as a function of the background level. Results are estimated with event planes from TPC, based on 20–60% collisions selected from 1.2×10^9 minimum bias events. RHIC beam use request for runs 18 and 19. The STAR Collaboration. May 15, 2017.

There will be possible the determination of the CME-signal with significance 5σ if 80% observed correlations is background.

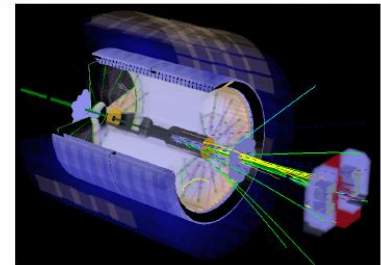
Future plans



Conceptual Design Report for the iTPC Upgrade
 The STAR Collaboration



The STAR Forward Calorimeter System and Forward Tracking System



Proposal May 2017

Phase-II of the beam energy scan program at RHIC. STAR 2020+ for study of cold QCD matter.

Detector upgrades for BES II

The three detector subsystems will be made for phase II of beam energy scan at RHIC: upgrade of inner sectors of TPC, endcap for time-of-light (TOF) and event plane detector (EPD).

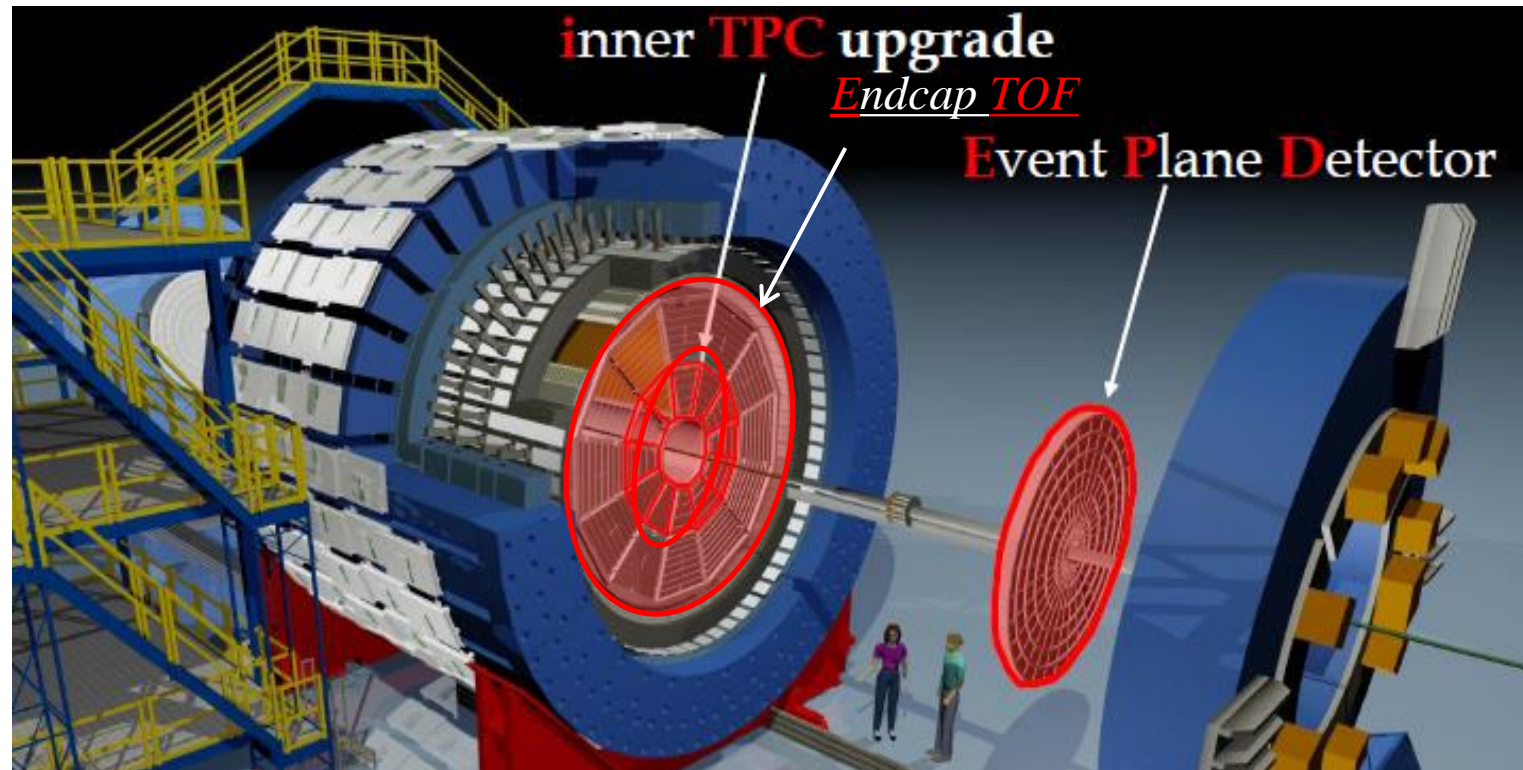


Fig. 25. View of the STAR detector with upgrades for phase II of BES at RHIC.

iTPC upgrade

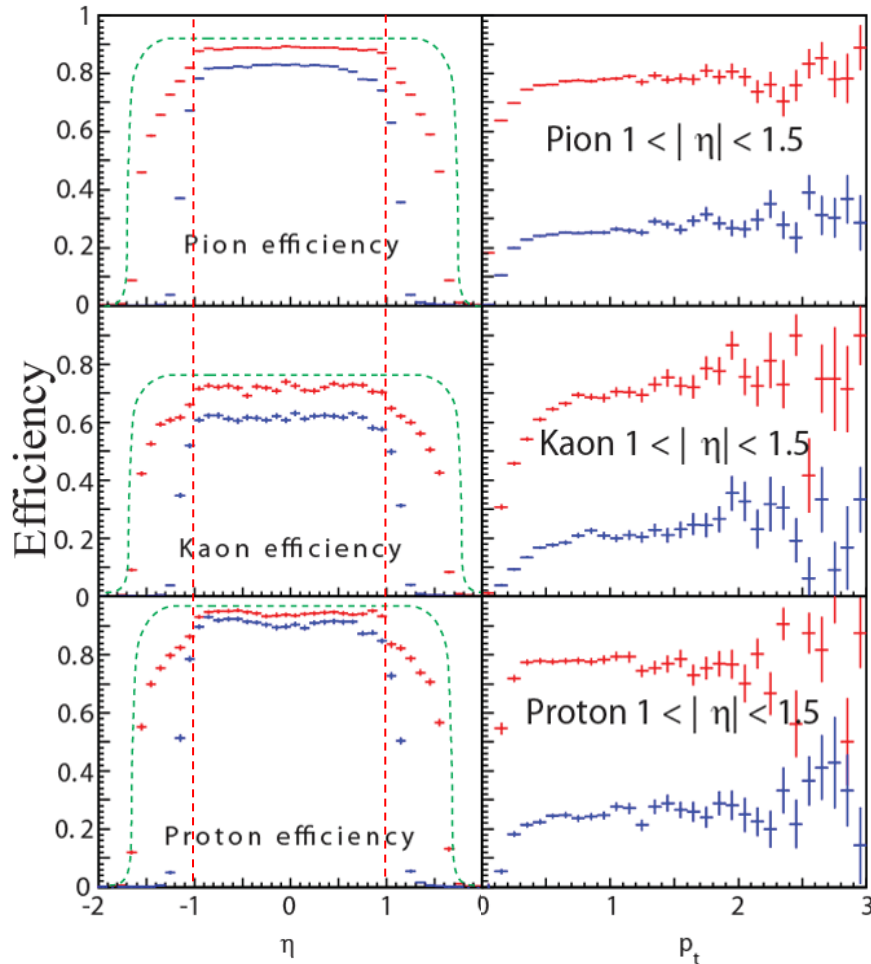


Fig. 26. Efficiency of charged particle identification as function of η (left) and p_T (right) for present TPC (blue points) and for iTPC (red points). The theoretical bound is shown by green lines for η -acceptance.

Major improvements are following:

- continues coverage (pad rows: 13 \rightarrow 40),
- improves dE/dx on 15–30%,
- extends $|\eta|$ coverage from 1.0 to 1.5,
- better momentum resolution,
- lowers p_T cut from 125 MeV/c to 60 MeV/c.

EP detector

The EPD is crucially important for study of (anti)hyperon polarization in nuclear collisions as well as for BES physics due to independent event plane measurement.

Major improvements are following:

- significant azimuthal and radial segmentation,
- better trigger and background reduction,
- extends $|\eta|$ coverage from $3.3 < |\eta| < 5.0$ to $2.1 < |\eta| < 5.1$,
- measure the centrality and event plane at forward rapidity,
- improves event plane resolution.

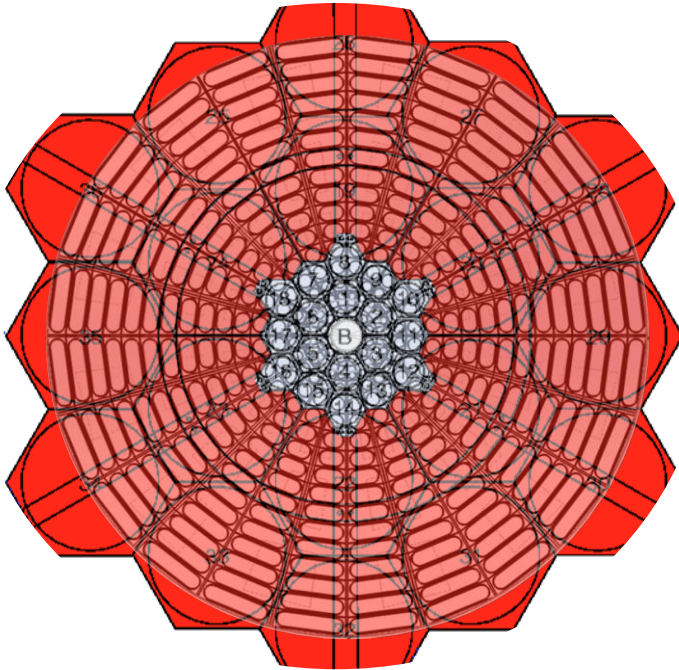


Fig. 27. Schematic view of EPD with respect to the existing beam-beam counter (BBC) subsystem. There will be 372 channels for EPD instead of 16 present channels for BBC.

eTOF detector

The eTOF is the joint project between STAR and CBM. This detector is important for fixed target program and complements the existing barrel TOF.

Major improvements are following:

- mid-rapidity particle identification in fixed target mode,
- extension of identification capabilities for π , p and K ,
- additional for bTOF ($-0.9 < |\eta| < 0.9$) η coverage: $-1.5 < \eta < -1.1$.

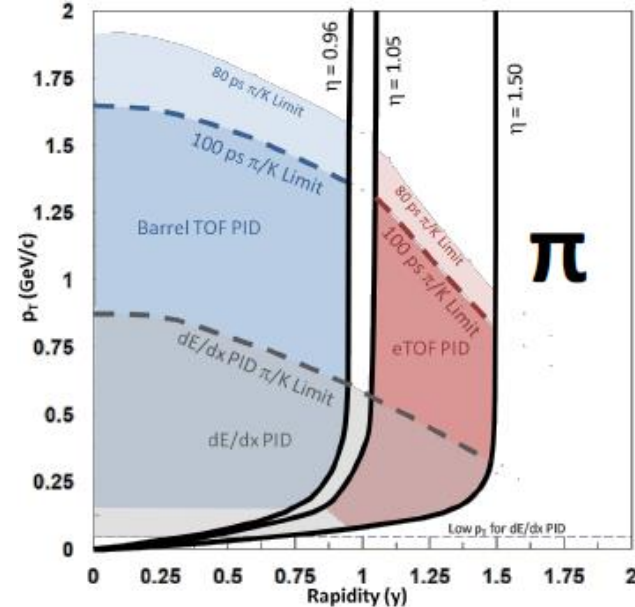
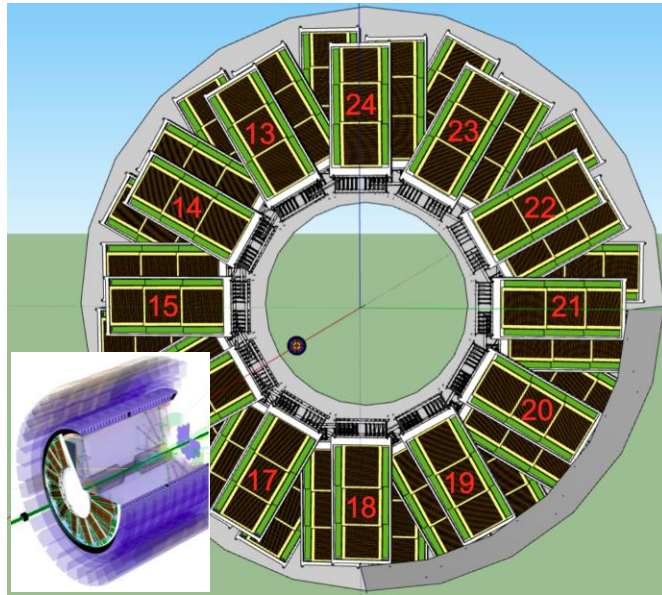


Fig. 28. Schematic view of eTOF detector (left), acceptance with identification capability for π at low- and intermediate p_T with the combination of iTPC and eTOF (right).

STAR 2020+: towards cold QCD

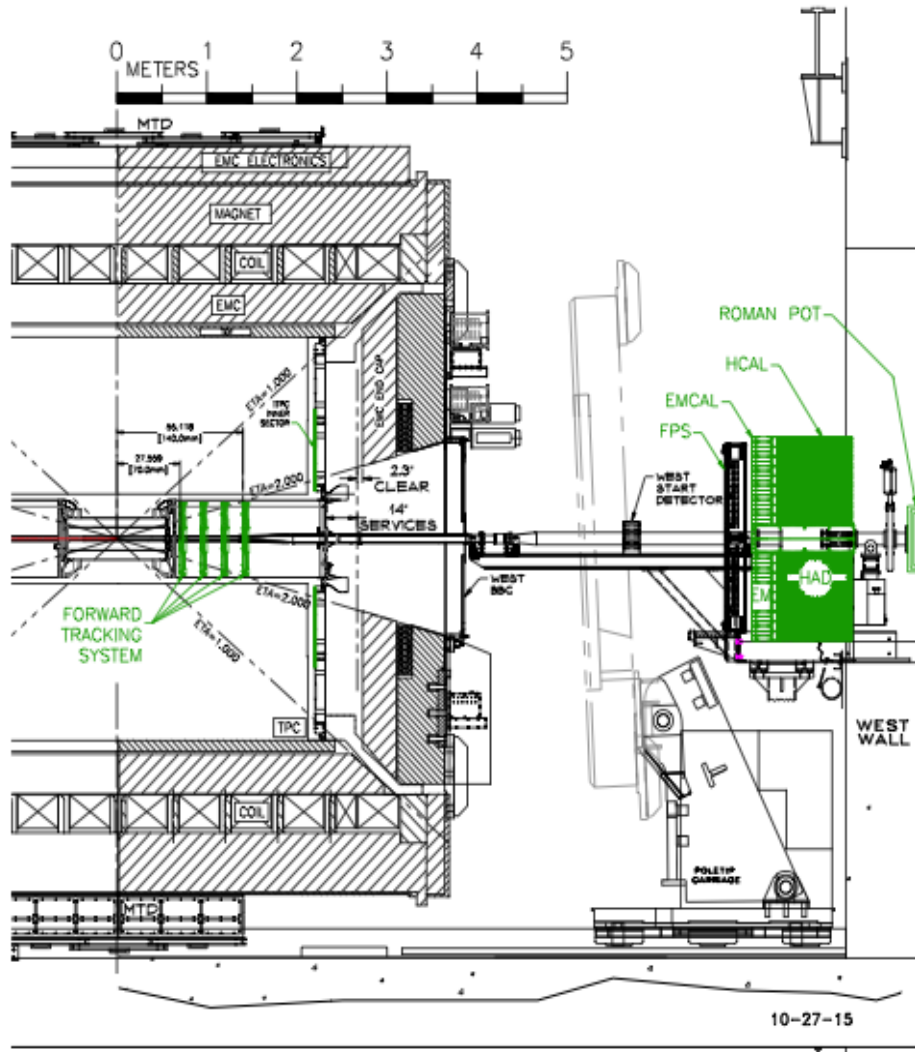


Fig. 29. Location of the forward calorimeter system (FCS) at the west side of the STAR detector.
The STAR forward calorimeter system and forward tracking system. Proposal, May 2017.

The RHIC cold QCD plan requires an upgrade to the forward rapidity ($2.5 < \eta < 4.5$) detection capabilities of STAR.

This upgrade allows the exploration of cold QCD physics in very high and low regions of Bjorken x as well as the longitudinal structure of the initial state and the temperature dependent transport properties of matter in nuclear collisions with help of measurements of

- azimuthal asymmetries,
- dihadron and h/γ -jet correlations,
- asymmetries in production of hadrons and jets,
- R_{pA} for direct γ and Drell–Yan process.

Summary

1. Present

- (anti) Λ hyperons are polarized in nuclear collisions and quark-gluon matter at RHIC is most vortical fluid even produced in the laboratory;
- v_1 indicates on the presence of a strong, initial electric field in asymmetric collisions;
- light (anti)nuclei and D^0 mesons show the collective behavior which agrees with general trends;
- quarkonia measurements in heavy ion collisions consistent with the expectations from the sequential melting hypothesis;
- azimuthal correlations with neutral triggers show the absence of path-length dependence for neutral pions and direct photons;
- semi-inclusive jet production demonstrate the possible reduction of medium-induced energy transport to large angles at RHIC with respect to the LHC.

The present stage in studies is the transition from the qualitative statements to the quantitative understanding in relativistic nuclear physics.

2. Future

- there are detail plans for physics studies and detector upgrades
- until 2020 (RHIC core program): precise study of sQGP within phase-II of the BES;
- after 2020: effects of QCD cold matter, longitudinal structure of initial conditions.

Thanks for you attention